# An achromatic approach to phase-based multi-modal imaging with conventional X-ray sources

**Marco Endrizzi,[1,*] Fabio A. Vittoria,[1] Gibril Kallon,[1] Dario Basta,[1] Paul C. Diemoz,[1] Alessandro Vincenzi,[2] Pasquale Delogu,[3,4] Ronaldo Bellazzini[2,3] and Alessandro Olivo[1]**

[1]*Department of Medical Physics and Biomedical Engineering, University College London, Gower Street, WC1E 6BT London, UK*

[2]*PIXIRAD Imaging Counters s.r.l., c/o INFN Pisa, Largo B. Pontecorvo 3, 56127 Pisa, Italy*

[3]*INFN, Pisa Section, Largo B. Pontecorvo 3, 56127 Pisa, Italy*

[4]*Dipartimento di Fisica, University of Pisa, Largo B. Pontecorvo 3, 56127 Pisa, Italy*

[*]*m.endrizzi@ucl.ac.uk*

**Abstract:** Compatibility with polychromatic radiation is an important requirement for an imaging system using conventional rotating anode X-ray sources. With a commercially available energy-resolving single-photon-counting detector we investigated how broadband radiation affects the performance of a multi-modal edge-illumination phase-contrast imaging system. The effect of X-ray energy on phase retrieval is presented, and the achromaticity of the method is experimentally demonstrated. Comparison with simulated measurements integrating over the energy spectrum shows that there is no significant loss of image quality due to the use of polychromatic radiation. This means that, to a good approximation, the imaging system exploits radiation in the same way at all energies typically used in hard-X-ray imaging.



**OCIS codes:** (110.7440) X-ray imaging; (100.5070) Phase retrieval.

## References and links

1. R. Fitzgerald, "Phase-sensitive x-ray imaging," Physics Today **53**(7), 23–26 (2000).
2. A. Bravin, P. Coan, and P. Suortti, "X-ray phase-contrast imaging: from pre-clinical applications towards clinics," Phys. Med. Biol. **58**(1), R1 (2013).
3. S. Wilkins, Y. Nesterets, T. Gureyev, S. Mayo, A. Pogany, and A. Stevenson, "On the evolution and relative merits of hard x-ray phase-contrast imaging methods," Phil. Trans. R. Soc. A **372**, 20130021 (2014).
4. U. Bonse and M. Hart, "An x-ray interferometer," Appl. Phys. Lett. **6**, 155 –156 (1965).
5. E. Foerster, K. Goetz, and P. Zaumseil, "Double crystal diffractometry for the characterization of targets for laser fusion experiments," Krist. Tech. **15**(8), 937–945 (1980).
6. A. Snigirev, I. Snigireva, V. Kohn, S. Kuznetsov, and I. Schelokov, "On the possibilities of x-ray phase contrast microimaging by coherent high-energy synchrotron radiation," Rev. Sci. Instrum. **66**(12), 5486–5492 (1995).
7. T. J. Davis, D. Gao, T. E. Gureyev, A. W. Stevenson, and S. W. Wilkins, "Phase-contrast imaging of weakly absorbing materials using hard X-rays," Nature **373**, 595–598 (1995).
8. V. N. Ingal and E. A. Beliaevskaya, "X-ray plane-wave topography observation of the phase contrast from a non-crystalline object," J. Phys. D: Appl. Phys. **28**, 2314–2317 (1995).
9. S. W. Wilkins, T. E. Gureyev, D. Gao, A. Pogany, and A. W. Stevenson, "Phase-contrast imaging using polychromatic hard x-rays," Nature **384**, 335–338 (1996).

10. D. Chapman, W. Thomlinson, R. E. Johnston, D. Washburn, E. Pisano, N. Gmür, Z. Zhong, R. Menk, F. Arfelli, and D. Sayers, "Diffraction enhanced x-ray imaging," Phys. Med. Biol. **42**, 2015–2025 (1997).
11. A. Olivo, F. Arfelli, G. Cantatore, R. Longo, R. H. Menk, S. Pani, M. Prest, P. Poropat, L. Rigon, G. Tromba, E. Vallazza, and E. Castelli, "An innovative digital imaging set-up allowing a low-dose approach to phase contrast applications in the medical field," Med. Phys. **28**, 1610–1619 (2001).
12. C. David, B. Nohammer, H. H. Solak, and E. Ziegler, "Differential x-ray phase contrast imaging using a shearing interferometer," Appl. Phys. Lett. **81**(17), 3287–3289 (2002).
13. L. Rigon, H.-J. Besch, F. Arfelli, R.-H. Menk, G. Heitner, and H. Plothow-Besch, "A new DEI algorithm capable of investigating sub-pixel structures," J. Phys. D: Appl. Phys. **36**, A107 (2003).
14. M. N. Wernick, O. Wirjadi, D. Chapman, Z. Zhong, N. P. Galatsanos, Y. Yang, J. G. Brankov, O. Oltulu, M. A. Anastasio, and C. Muehleman, "Multiple-image radiography," Phys. Med. Biol. **48**, 3875–3895 (2003).
15. F. Pfeiffer, T. Weitkamp, O. Bunk, and C. David, "Phase retrieval and differential phase-contrast imaging with low-brilliance X-ray sources," Nat. Phys. **2**, 258–261 (2006).
16. W. Yashiro, Y. Terui, K. Kawabata, and A. Momose, "On the origin of visibility contrast in x-ray talbot interferometry," Opt. Express **18**(16), 16890–16901 (2010).
17. K. S. Morgan, D. M. Paganin, and K. K. W. Siu, "X-ray phase imaging with a paper analyzer," Appl. Phys. Lett. **100**(12), 124102 (2012).
18. D. Pelliccia, L. Rigon, F. Arfelli, R.-H. Menk, I. Bukreeva, and A. Cedola, "A three-image algorithm for hard x-ray grating interferometry," Opt. Express **21**(16), 19401–19411 (2013).
19. A. Olivo and R. Speller, "A coded-aperture technique allowing x-ray phase contrast imaging with conventional sources," Appl. Phys. Lett. **91**(7), 074106 (2007).
20. P. R. Munro, K. Ignatyev, R. D. Speller, and A. Olivo, "Phase and absorption retrieval using incoherent X-ray sources," Proc. Natl. Acad. Sci. USA **109**(35), 13922–13927 (2012).
21. M. Endrizzi, P. C. Diemoz, T. P. Millard, J. L. Jones, R. D. Speller, I. K. Robinson, and A. Olivo, "Hard x-ray dark-field imaging with incoherent sample illumination," Appl. Phys. Lett. **104**(2), 024106 (2014).
22. C. K. Hagen, P. R. T. Munro, M. Endrizzi, P. C. Diemoz, and A. Olivo, "Low-dose phase contrast tomography with conventional x-ray sources," Med. Phys. **41**(7), 070701 (2014).
23. M. Endrizzi, F. A. Vittoria, P. C. Diemoz, R. Lorenzo, R. D. Speller, U. H. Wagner, C. Rau, I. K. Robinson, and A. Olivo, "Phase-contrast microscopy at high x-ray energy with a laboratory setup," Opt. Lett. **39**(11), 3332–3335 (2014).
24. T. Thuering, W. C. Barber, Y. Seo, F. Alhassen, J. S. Iwanczyk, and M. Stampanoni, "Energy resolved x-ray grating interferometry," Appl. Phys. Lett. **102**(19), 191113 (2013).
25. G. Pelzer, T. Weber, G. Anton, R. Ballabriga, F. Bayer, M. Campbell, T. Gabor, W. Haas, F. Horn, X. Llopart, N. Michel, U. Mollenbauer, J. Rieger, A. Ritter, I. Ritter, P. Sievers, S. Wölfel, W. S. Wong, A. Zang, and T. Michel, "Grating-based x-ray phase-contrast imaging with a multi energy-channel photon-counting pixel detector," Opt. Express **21**(22), 25677–25684 (2013).
26. M. Das and Z. Liang, "Spectral x-ray phase contrast imaging for single-shot retrieval of absorption, phase, and differential-phase imagery," Opt. Lett. **39**(21), 6343–6346 (2014).
27. R. Bellazzini, G. Spandre, A. Brez, M. Minuti, M. Pinchera, and P. Mozzo, "Chromatic x-ray imaging with a fine pitch cdte sensor coupled to a large area photon counting pixel asic," J. Instrum. **8**(02), C02028 (2013).
28. P. R. Munro, K. Ignatyev, R. D. Speller, and A. Olivo, "The relationship between wave and geometrical optics models of coded aperture type x-ray phase contrast imaging systems," Opt. Express **18**, 4103 (2010).
29. P. R. T. Munro, K. Ignatyev, R. D. Speller, and A. Olivo, "Source size and temporal coherence requirements of coded aperture type x-ray phase contrast imaging systems," Opt. Express **18**, 19681 (2010).
30. P. C. Diemoz and A. Olivo, "On the origin of contrast in edge illumination x-ray phase-contrast imaging," Opt. Express **22**(23), 28199–28214 (2014).
31. M. Endrizzi and A. Olivo, "Absorption, refraction and scattering retrieval with an edge-illumination-based imaging setup," J. Phys. D: Appl. Phys. **47**(50):505102, 2014.
32. K. Ignatyev , P. R. T. Munro, R. D. Speller and A. Olivo, "Effects of signal diffusion on x-ray phase contrast images, " Rev. Sci. Instrum. **82**(7), 073702 (2011).
33. A. Vincenzi, P. L. de Ruvo, P. Delogu, R. Bellazzini, A. Brez, M. Minuti, M. Pinchera, and G. Spandre, "Energy characterization of pixirad-1 photon counting detector system," J. Instrum. **10**(04), C04010 (2015).
34. R. Bellazzini, A. Brez, G. Spandre, M. Minuti, M. Pinchera, P. Delogu, P. de Ruvo, and A. Vincenzi, "Pixie iii: a very large area photon-counting cmos pixel asic for sharp x-ray spectral imaging," J. Instrum. **10**(01), C01032 (2015).

## 1. Introduction

Thanks to its sensitivity to the phase shifts suffered by the X-ray beam when it passes through a sample, X-ray Phase-Contrast Imaging (XPCI) extends the potential of conventional radiography to applications where absorption contrast is insufficient to allow the visualization of the

details of interest [1, 2]. XPCI can be widely applied to fields as diverse as medicine, security screening, biology and materials science. Several approaches have been developed to perform XPCI using both synchrotron radiation and X-ray tubes [3–18].

Edge illumination (EI) [11] and its area-imaging implementation, often referred to as coded-aperture [19], are XPCI techniques that enable the quantitative retrieval of amplitude, phase and ultra-small-angle scattering information under practically negligible coherence conditions [20, 21]. These methods are well suited for implementation with all types of sources including synchrotron radiation [11], rotating anode [19, 20, 22] and microfocal [23] X-ray tubes.

We present here an experimental study of the achromatic properties of edge-illumination by using a laboratory set-up based on a rotating anode X-ray tube and an imaging detector with energy-resolved single-photon counting capability. While in other XPCI approaches, such as grating interferometry, it was shown that the performance of the imaging system varies significantly across the energy range covered by typical polychromatic X-ray tube spectra [24, 25], this is not the case for EI. We show that the illumination function, describing the characteristics of the imaging system, has little variation in the energy range explored ($5-40$ keV). In addition, by comparison with a simulated integration over the energy spectrum, we find that there is no significant image quality loss when more conventional integrating detector technologies are used with our method. On the one hand this means that a simple set-up allows for an efficient exploitation of the wide energy spectrum produced by rotating anode X-ray tubes. On the other, since the imaging system transmits all wavelengths in the same way, the use of an energy-resolving detector opens the way to edge-illumination multi-energy X-ray phase-contrast imaging [26].

## 2. Methods

We used a typical set-up for the laboratory implementation of edge-illumination XPCI, with the inclusion of a detector with single-photon-counting and energy discrimination capabilities. This is PiXirad, an innovative X-ray imaging sensor that counts individually the X-ray photons and selects them according to their energy, producing a two-bins image with a single exposure. The energy selection occurs in real time and at radiographic imaging speed (GHz). The building blocks of the imaging system are two-side buttable semiconductor radiation detectors (pixellated CdTe) coupled to a large area ASIC [27]. As sketched in Fig. 1, the X-ray beam is shaped by the pre-sample mask into an array of independent laminar beams, aligned in such a way that each of them impinges on an absorbing edge. A different fraction of each laminar beam will reach the detector or be stopped by the second mask, depending upon the properties of the sample. In this particular set-up, the detector counts the number of detected photons and discriminates their energy. In a typical laboratory experiment, relatively large sources and short distances are used, which allows image formation to be described by geometrical optics [28–30]. The intensity recorded by the image receptor can be written as [21]:

$$\frac{I(x)}{I_0} = (L * O)(x - \Delta x_R)t \tag{1}$$

which holds independently for each pixel. $I_0$ is the intensity passing through the pre-sample aperture, $L$ the illumination function, $O$ the scattering distribution characteristic of the sample, $t$ the fraction of intensity transmitted, $\Delta x_R = -\Delta\theta_R z_{od}$ the beam shift induced by refraction in the sample (where $z_{od}$ is the distance between the object and the detector) and $*$ indicates the convolution. The $x$ direction is orthogonal to the beam propagation axis and to the apertures, i.e. is the direction along which the system is sensitive to refraction.

By using the energy-resolving capabilities of the PiXirad detector, the contributions to the total intensity coming from X-rays of different energy can be separated. This can be included

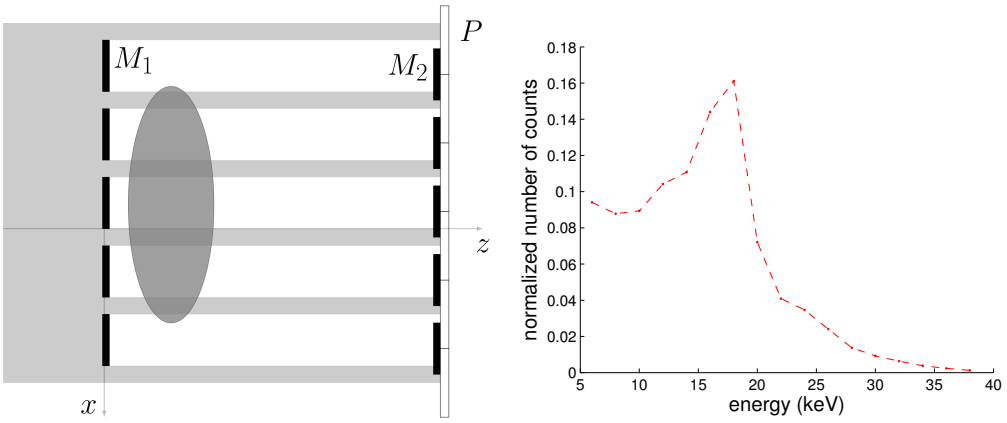


(a) (b)

Fig. 1. (a) Schematic of the experimental set-up: the polychromatic X-ray beam generated by a rotating anode X-ray source is shaped by the pre-sample mask $M_1$, interacts with the sample and is analysed by the detector mask $M_2$ before being detected by an energy-discriminating single-photon-counting detector pixel $P$. (b) Energy distribution of the radiation directly measured with the detector used for this study.

in Eq. (1) by rewriting it as:

$$\frac{I(x,e)}{I_0(e)} = (L(e) * O(e))(x - \Delta x_R(e))t(e) \tag{2}$$

where now all quantities characterising the imaging system, $L(x,e)$ and $I_0(e)$, and the sample, $t(e)$, $\Delta x_R(e)$ and $O(x,e)$ are expressed as a function of the X-ray energy $e$.

Intensity projections $I_{1,2,3}$ can be acquired by setting the masks' displacement to $x_2 = 0$ and $x_1 = -x_3$, and the retrieval, described in a previous work [21], applied at each energy window:

$$\begin{cases} t(e) &= \frac{2x_1}{A_{MN}(e)} \sqrt{\frac{\pi}{D(e)+C(e)}} I_2(e) \exp\left[\frac{1}{2^4} \frac{(D(e)-C(e))^2}{D(e)+C(e)}\right] \\ \Delta x_R(e) &= \frac{x_1}{2} \frac{D(e)-C(e)}{D(e)+C(e)} \\ \sigma_M^2(e) &= \frac{2x_1^2}{D(e)+C(e)} - \sigma_N^2(e) \end{cases} \tag{3}$$

where $C(e) = -2\ln(I_1(e)/I_2(e))$ and $D(e) = -2\ln(I_3(e)/I_2(e))$. Furthermore, the iterative correction procedure which is used to take into account the presence of an offset in the illumination function [31], can also be applied to the measurements corresponding to each energy bin.

The experimental set-up is based on a rotating anode X-ray tube (Mo target, Rigaku MM007) and an energy-resolving single-photon-counting detector (Pixirad-1 X-ray detection system, Pixirad Imaging Counters s.r.l., Italy). The masks were manufactured by Creatv Microtech (Potomac, MD) and had pitches $p_1 = 79$ and $p_2 = 98$ $\mu$m and apertures $a_1 = 23$ and $a_2 = 29$ $\mu$m, respectively for the pre-sample $M_1$ and detector $M_2$ masks. They were made of a 150 $\mu$m thick gold layer, electroplated on a graphite substrate, with a field of view of $4.8 \times 4.8$ cm. The distances between the source and $M_1$, and between $M_1$ and $M_2$, were 160 and 40 cm respectively. The Pixirad-1 pixels are hexagonal [27] which results in two different pitches, 52 and 60 $\mu$m, along the two orthogonal directions in the detector plane. For this experiment we oriented the detector with the 52 $\mu$m pitch aligned with the $x$ direction and we also skipped every other column by using a line-skipped [32] mask design. The resulting imaging system is

not affected by the hexagonal shape of the detector pixels, i.e. it behaves in exactly the same way as if the pixels were squared. The X-ray tube was operated at 40 kVp and had a focal spot of about 70 $\mu$m. The energy threshold of the detector was scanned between 5 and 40 keV so as to count photons with 2 keV bins over the entire energy spectrum of the source [33].

To compare the performance of the imaging system with and without energy-resolving capabilities, we did the following. The images were retrieved by using the illumination functions and intensity projections recorded at each energy bin and applying Eq. (3), followed by the iterative procedure to correct for the offset of the illumination function. After the retrieval, images corresponding to different energies were summed (weighting with the X-ray spectrum), and the result was compared to the images calculated by using the integral illumination function and intensity projections (obtained by summing the detected intensities in all the energy bins) and performing a single retrieval. The signal, taken as the maximum difference between the positive and the negative peak, and the noise, taken as the standard deviation of a region of interest in the vicinity of the sample, were measured in each refraction image, and the signal-to-noise ratios compared. Energies below 13 keV were discarded because a relatively large number of multiple counts were contained in these energy bins. This was primarily due to charge-sharing [33]: if the charge carriers generated by a single interacting photon are collected by several pixels, this results in multiple lower-energy counts. In the experimental conditions we used, one would expect only 7% of the total number of photons to be at energies below 13 keV, which means that their removal has limited impact on the performance analysis. The energy bins above 35 keV were also discarded during the analysis, due to the extremely limited statistics. It should be noted, however, that the problem of charge sharing can be substantially mitigated by using a more sophisticated read-out scheme [34].

The samples used in this study were cylinders of various materials: sapphire (diameter 250 $\mu$m), PET (diameter 100 $\mu$m), PEEK (diameter 150 $\mu$m) and nylon (diameter 300 $\mu$m). A cylindrical cross-section box with a thickness of about 800 $\mu$m, filled with 10 $\mu$m diameter borosilicate spheres, was used for the ultra-small-angle X-ray scattering measurements.

## 3. Results

Figure 2 shows the retrieved images for the sapphire cylinder sample. Refraction is shown in Figs. 2(a)-2(c), while transmission in Figs. 2(d)-2(f). Three energy bins are reported: $13-15$ keV in Figs. 2(a) and 2(d); $17-19$ keV in Figs. 2(b) and 2(e); $21-23$ keV in Figs. 2(c) and 2(f). A higher contrast can be observed for lower energy while statistics is best in the central images, due to the presence of molybdenum line emissions.

The comparison between the SNR obtained using the energy-resolved data $SNR_e$ and the integrated data $SNR_i$ showed that the two processes produce comparable results to within a few percent variation. The obtained values of $\{SNR_e, SNR_i\}$ were $\{46, 50\}$ for the sapphire sample, $\{23.2, 23.5\}$ for the nylon sample, $\{17.5, 17.3\}$ for the PEEK sample and $\{14.6, 15.3\}$ for the PET sample, respectively.

Due to the use of large apertures and source size, with relatively short propagation distances, all the wavelengths are transmitted in the same way by the imaging system. This means that the whole energy spectrum is used to generate contrast in the projection images and therefore that edge-illumination- and coded-aperture-based systems can be considered achromatic. This is experimentally demonstrated in Fig. 3, where the parameters characterising the illumination function are measured across the energy spectrum at 1 keV intervals. The parameters show little variation as a function of energy, this includes the offset of the illumination function, which originates from two principal sources. One is the partial transmission of X-rays through the absorbing septa of the masks, and the other is the presence of long tails in the intensity distribution of the source. The masks used in this experiment were relatively thick, and no

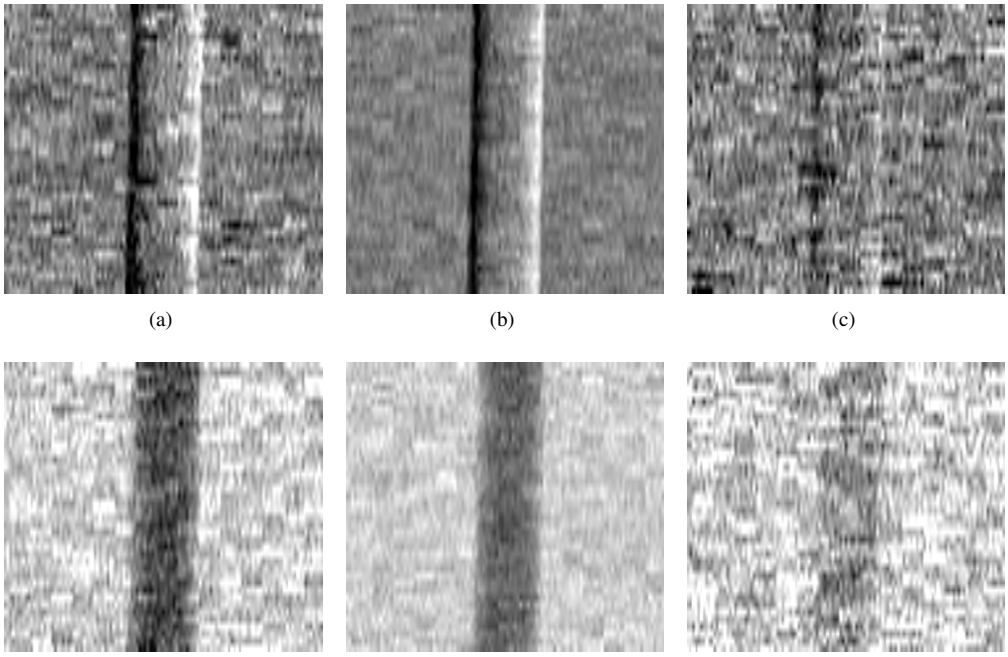

(a) (b) (c)

(d) (e) (f)

Fig. 2. Retreived (a)-(c) refraction and (d)-(f) transmission images of the sapphire cylinder sample. Three energy bins are shown here: $13-15$ keV (a) and (d), $17-19$ keV (b) and (e), $21-23$ keV (c) and (f). Contrast is higher for lower energies while statistics is best for the central energy interval, corresponding to the molybdenum line emission.

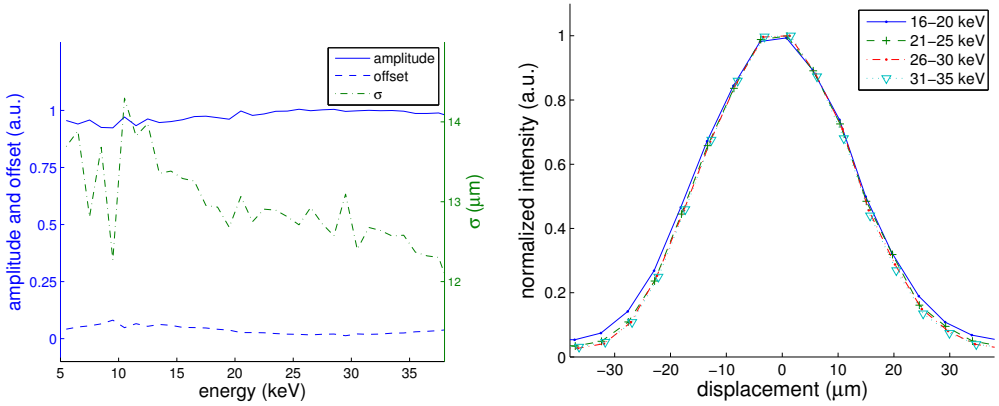


(a) (b)

Fig. 3. Illumination function of the imaging system measured at different energies by using an energy-resolving single-photon-counting imaging detector. (a) Parameters measured at 1 keV intervals across the whole energy spectrum of the X-ray source and (b) visual comparison of the illumination functions measured dividing the counts into four energy intervals $16-20$, $21-25$, $26-30$ and $31-35$ keV.

significant dependence upon the energy was observed for the offset: we therefore attribute the small offset that is still observed in these data primarily to the long tails in the shape of the focal spot. The relative amount with which each wavelength contributes to the contrast in the final image depends also on the variation in efficiency of the detector as a function of energy. This can be considered uniform in our experiment as the probability of interaction within 650 $\mu$m of CdTe is practically 100% up to 40 keV.

The same concepts can be applied for the ultra-small-angle X-ray scattering signal. Figure 4 shows the comparison between signal $S_{i,e}$ and backgrounds $BG_{i,e}$ obtained by using the integrated and the energy-resolved data. A small shift, as well as a slight change in width, can potentially be observed between $S_i$ and $S_e$. This effect is, however, very small if compared to the full width of the distribution of both signals, making it difficult to separate it from the random fluctuations. While the quantitative equivalence of the results is demonstrated by the histogram

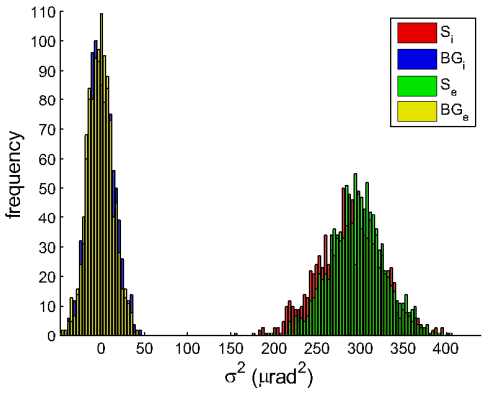


Fig. 4. Ultra-small-angle X-ray scattering, comparison between the signals obtained using the integrated $S_i$ and the energy-resolved $S_e$ data, and the corresponding backgrounds.

in Fig. 4, the images can also be visually compared in Fig. 5. The integrated data are shown in Fig. 5(a) and the energy-resolved data in Fig. 5(b). By defining the signal-to-noise ratio as

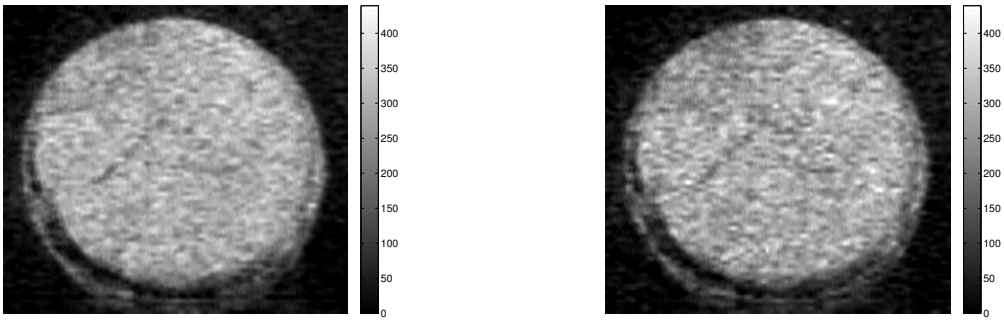

(a) (b)

Fig. 5. Visual comparison between (a) integrated and (b) energy-resolved data for the ultra-small-angle scattering image of the microspheres sample. Also by visual comparison the two images appear very similar one to each other.

the average of $S_{i,e}$ divided by the sum in quadrature of the standard deviations of $S_{i,e}$ and $BG_{i,e}$,

we obtain $SNR_i = 6.9$ and $SNR_e = 7.1$ for the integral and the energy-resolved measurement respectively.

## 4. Conclusions

We experimentally investigated how an edge-illumination based multi-modal phase-contrast imaging system responds to radiation at different X-ray energies by exploiting the spectroscopic capabilities of the PiXirad detector. The illumination function of the system showed minimal dependence on the X-ray energy in the range $5-40$ keV. This means that the imaging system generates contrast at all wavelengths simultaneously and the energy dependence of the signal is due to the sample itself, while the imaging system responds to different energies in the same way. This offers the possibility of performing multi-energy X-ray phase-contrast imaging by means of edge-illumination, thereby exploiting the full broadband of conventional X-ray tube sources. A comparison between a measurement simulating the integration over the energy spectrum and an energy-resolved one, demonstrated that very similar image quality is obtained, thus confirming that no significant losses are caused by the use of more widely available integrating detector technologies.


## Acknowledgments

This work was supported by the UK Engineering and Physical Sciences Research Council Grant EP/I021884/1 and by the UK Science and Technology Facilities Council Grant ST/L502662/1. ME and PCD are supported by Marie Curie Career Integration Grant within the Seventh Framework Programme of the European Union PCIG12-GA-2012-334056 and PCIG12-GA-2012-333990.